

# Enhanced photoresponse in MoTe<sub>2</sub> photodetectors with asymmetric graphene contacts

*Xia Wei, Faguang Yan, Quanshan Lv, Wenkai Zhu, Ce Hu, Amalia Patanè and Kaiyou Wang\**

Mr. X. Wei, Dr. F. Yan, Mr. Q. Lv, Mr. W. Zhu, Mr. C. Hu and Prof. K. Wang

State Key Laboratory of Superlattices and Microstructures, Institute of Semiconductors, Chinese Academy of Sciences, Beijing 100083, P. R. China

Center of Materials Science and Optoelectronics Engineering, University of Chinese Academy of Sciences, Beijing 100049, P. R. China

Center for Excellence in Topological Quantum Computation, University of Chinese Academy of Science, Beijing 100049, P. R. China

E-mail: [kywang@semi.ac.cn](mailto:kywang@semi.ac.cn)

Prof. A. Patanè

State Key Laboratory of Superlattices and Microstructures, Institute of Semiconductors, Chinese Academy of Sciences, Beijing 100083, China

School of Physics and Astronomy, University of Nottingham, Nottingham NG7 2RD, United Kingdom

**Keywords:** asymmetric graphene contacts, MoTe<sub>2</sub>, van der Waals heterostructure, built-in electric field, enhanced photoresponse

**Atomically thin two dimensional (2D) materials are promising candidates for miniaturized high-performance optoelectronic devices. Here, we report on multilayer MoTe<sub>2</sub> photodetectors contacted with asymmetric electrodes based on *n*- and *p*-type graphene layers. The asymmetry in the graphene contacts creates a large ( $E_{bi} \sim 100$  kV cm<sup>-1</sup>) built-in electric field across the short ( $l = 15$  nm) MoTe<sub>2</sub> channel, causing a high and broad ( $\lambda = 400$  to 1400 nm) photoresponse even without any externally applied voltage. Spatially resolved photovoltage maps reveal an enhanced photoresponse and larger built-in electric field in regions of the MoTe<sub>2</sub> layer between the two graphene contacts. Furthermore, a fast ( $\sim 10$   $\mu$ s) photoresponse is achieved in both the photovoltaic and photoconductive operation modes of the junction. Our findings could be extended to other 2D materials and offer prospects for the implementation of asymmetric graphene contacts in future low-power optoelectronic applications.**

## 1. Introduction

Two dimensional (2D) van der Waals crystals have received great attention due to their excellent properties and versatility for a wide range of potential applications in optoelectronics.<sup>[1,2]</sup> In particular, transition metal dichalogenides (TMDs) with their finite and tunable bandgap energy (from  $E_g = 1.1$  to  $2.1$  eV) and strong light absorption offer opportunities for a variety of optoelectronic devices.<sup>[2-4]</sup> Amongst the TMDs, MoTe<sub>2</sub> is an attractive semiconductor. In the monolayer form, it has a direct bandgap,  $E_g = 1.10$  eV at room temperature, larger than that of bulk MoTe<sub>2</sub>, which has an indirect bandgap ( $E_g = 0.85$  eV).<sup>[5-7]</sup> Thus, unlike other TMDs, such as MoS<sub>2</sub> and WS<sub>2</sub>, photodetectors based on MoTe<sub>2</sub> can have a broadband photoresponse that extends from the visible (VIS) to the near infrared (NIR) spectral range.<sup>[8-10]</sup> In particular, in MoTe<sub>2</sub>-based field effect transistors (FETs), the photoresponsivity ( $R$ ) can be enhanced by a photogating effect and achieve values of up to  $R = 24$  mA W<sup>-1</sup> under illumination with NIR light.<sup>[9]</sup> Although Si has a similar bandgap to that of MoTe<sub>2</sub>, its absorption coefficient in the NIR spectral range is smaller than that of MoTe<sub>2</sub>: for Si, the absorption coefficient is  $8.17$  cm<sup>-1</sup> at  $\lambda = 1064$  nm, which is smaller than that for MoTe<sub>2</sub> ( $4.9 \times 10^4$  cm<sup>-1</sup>).<sup>[11]</sup>

In contrast to traditional bulk semiconductors such as Si, Ge or III-V compounds, 2D vdW crystals have surfaces that are free of dangling bonds.<sup>[2]</sup> This unique feature arises from their atomic structure: the atoms are arranged into layers that are held together by strong covalent in-plane bonds; in contrast, in the out-of-plane direction, the atomic layers interact with weak vdW interactions. This offers opportunities to combine them with other materials without the limitations of lattice mismatch that apply to covalent crystals.<sup>[2,12]</sup> For example, MoTe<sub>2</sub> has been used in different multilayer structures: in MoTe<sub>2</sub>/MoS<sub>2</sub> heterojunctions, the on/off photocurrent

ratio can reach values of about 780;<sup>[13]</sup> also, the photoconductive gain in MoTe<sub>2</sub>/graphene heterostructures can be as large as  $4.69 \times 10^8$ .<sup>[9]</sup> More generally, asymmetric contact barriers between two electrodes and a 2D vdW crystal can be exploited to construct high performance photodetectors.<sup>[14-21]</sup> Au and In Schottky contacts to a 2D material can be used to realize self-powered photodetectors with high photoresponsivity ( $R = 110 \text{ mA W}^{-1}$ ).<sup>[14]</sup> Also, graphene can form a clean interface with 2D materials and its near perfect optical transparency makes it suitable for use as the top electrode of vertical heterostructure photodetectors.<sup>[22-25]</sup> Au/MoTe<sub>2</sub>/graphene vertical heterostructures have good photoresponsivity and photoreponse time of about 96 ms.<sup>[15]</sup> However, the photoresponse of 2D vdW heterostructure devices in the current literature remain still slow due to relatively long optically active channels and/or charge traps at the metal/2D material interface.<sup>[14,15,26-29]</sup> Thus, both the length of the channel and the quality of the contacts should be carefully chosen to optimize the photoresponse.

In this study, we report on photodetectors based on MoTe<sub>2</sub> with vertical asymmetric graphene contacts. We use *p*-type graphene grown by chemical vapour deposition (CVD) as the top contact and *n*-type exfoliated graphene as the bottom contact. This asymmetry in the graphene contacts is adopted to break the mirror symmetry of the internal electric field profile, thus creating a large built-in electric field  $E_{bi}$ . This feature combined with the short length of the MoTe<sub>2</sub> optically active channel enables an efficient and fast photoresponse. The heterostructure exhibits a high and broad spectral photoresponse from the VIS to the NIR range of the electromagnetic spectrum ( $\lambda = 400 - 1400 \text{ nm}$ ) without any external applied voltage: the photoresponsivity is  $R = 12.38 \text{ mA W}^{-1}$  at  $\lambda = 1064 \text{ nm}$  and  $R = 27.64 \text{ mA W}^{-1}$  at  $\lambda = 550 \text{ nm}$ . Through scanning photovoltaic mapping, an enhanced light absorption is clearly observed in the overlapping region of the graphene and MoTe<sub>2</sub> layers. Furthermore, because of the short ( $l$

= 15 nm) MoTe<sub>2</sub> channel between the top and bottom graphene contacts in the vertical heterostructure, the response time of the device can be as short as ~ 6.15 μs, which is 1-3 orders of magnitude faster than that reported before for MoTe<sub>2</sub>-based photodetectors.<sup>[1,9,15,30,31]</sup>

## 2. Results and discussion

**Figure 1(a)** shows the schematic layout of our MoTe<sub>2</sub>-graphene based photodetectors. To fabricate the MoTe<sub>2</sub>-graphene heterostructure, a multilayer graphene flake was first mechanically exfoliated from a bulk crystal using adhesive tape and then transferred onto a Si/SiO<sub>2</sub> substrate (300 nm-thick SiO<sub>2</sub>).<sup>[32,33]</sup> Using the same mechanical exfoliation and transfer method, a flake of MoTe<sub>2</sub> was then transferred onto the bottom graphene layer. Finally, a microstamp of CVD-graphene was transferred on top of the MoTe<sub>2</sub> flake to create the top electrode.<sup>[33]</sup> Metallic contacts (Ta/Au) were fabricated on the substrate using standard photoetching, magnetron sputtering and lift off. Single crystals of 2H-MoTe<sub>2</sub> were purchased from HQ graphene (Netherlands); CVD-grown graphene was provided by G-CVD (Xiamen, China) and the bulk graphite was purchased from 2D Semiconductors (US). All mechanical exfoliation and transfer processes were conducted inside a glove box.

**Figure 1(b)** shows the atomic force microscopy (AFM) image of one of our devices. The large and uniform exfoliated multi-layer graphene serves as a bottom electrode and has a thickness of 3.6 nm; the MoTe<sub>2</sub> flake has a thickness of about 15 nm; the top CVD-graphene layer corresponds to single layer graphene. Raman spectroscopy studies were conducted to assess the quality of the individual flakes and heterostructure over an extended frequency range (from 200 to 2800 cm<sup>-1</sup>) with an excitation laser wavelength  $\lambda = 532$  nm and power  $P = 100$  μW. A large magnification (100 ×) objective lens was used to focus the laser to a spot diameter

of 1.5  $\mu\text{m}$  and probe different regions, including the  $\text{MoTe}_2$ , exfoliated graphene, CVD-graphene and the region where all layers overlap.

Figure 1(c) shows typical Raman spectra of our samples. The Raman spectrum for the isolated  $\text{MoTe}_2$  flake shows two Raman-active modes: the  $E_{2g}^I$  mode at  $232.14\text{ cm}^{-1}$  and the  $B_{2g}^I$  mode at  $288.40\text{ cm}^{-1}$ , as observed in the literature.<sup>[26]</sup> For bulk  $\text{MoTe}_2$ , only the  $E_{2g}^I$  mode is observed (**Figure S1(a)**), consistent with previous reports.<sup>[5,7]</sup> The difference between the bulk and 2D layers is assigned to the breakup of the translation crystal symmetry in few layer  $\text{MoTe}_2$ .<sup>[9]</sup> In the Raman spectra of CVD and exfoliated graphene, the most intense features are the G and 2D peaks. The 2D peak from CVD graphene is approximately twice more intense than the G peak, confirming that CVD graphene is single layer.<sup>[34]</sup> In contrast, the G peak for exfoliated graphene is higher than the 2D peak, indicating that the flake is multilayer, in agreement with the AFM data. Furthermore, the Raman spectrum of exfoliated graphene reveals an additional stronger peak at  $2716.4\text{ cm}^{-1}$ , as also reported in the literature for multilayer graphene.<sup>[34-36]</sup> The peak is assigned to a  $q_{11}$  double-resonance Raman process.<sup>[35]</sup> In the Raman spectra of the vertical overlapping region, all the above peaks can be clearly observed, demonstrating the good quality of the heterostructure.

To investigate the electrical properties of our devices, the current,  $I_{ds}$ , was measured for different voltages,  $V_{ds}$ , applied between the drain (top CVD graphene) and source (bottom exfoliated graphene) contacts. All the electrical measurements were carried out in vacuum ( $\sim 5\text{ mbar}$ ) at room temperature. Figure 1(d) shows the  $I_{ds} - V_{ds}$  curves in the dark and under illumination: in the dark, the  $I_{ds} - V_{ds}$  curve shows nonlinear rectifying characteristics, consistent with asymmetric contact barriers between the  $\text{MoTe}_2$  flakes and the two graphene electrodes. Under continuous-wave laser illumination ( $\lambda = 1064\text{ nm}$ ), the current increases and the  $I_{ds} - V_{ds}$

shows a clear photovoltaic effect. For comparison, we fabricated photodetectors based on MoTe<sub>2</sub> with symmetric graphene contacts. In this case, the rectification behavior is not observed or is much smaller (inset of Figure 1(d)).

We now examine in detail the photoresponse properties of our photodetectors. **Figure 2(a)** shows the  $I_{ds} - V_{ds}$  characteristics with 1064 nm laser illumination at powers ranging from  $P = 0$  to  $6.25 \text{ W cm}^{-2}$ . The photocurrent,  $I_{ph}$ , is defined as  $I_{ph} = |I_{light} - I_{dark}|$  where  $I_{light}$  and  $I_{dark}$  are the currents measured with and without illumination, respectively. As shown in Figure 2(b), the photocurrent  $I_{ph}$  increases with increasing  $P$ , revealing a sublinear behavior, *i.e.*  $I_{ph} \propto P^\beta$ , where  $\beta$  increases from 0.855 to 0.911 when  $V_{ds}$  decreases from 0 to -0.20 V. Thus even without any applied source-drain voltage, the photo-generated electron-hole pairs can be effectively separated by the built-in electric field of the heterostructure to generate a photocurrent. Also, although  $\beta$  increases with decreasing  $V_{ds}$ , its value remains always smaller than 1. This is the fingerprint of a photoconductivity gain that is influenced by charge traps in the layers and/or their interfaces.<sup>[9,37,38]</sup> A similar phenomenon was reported in heterostructures based on different vdW crystals, such as WS<sub>2</sub>/MoS<sub>2</sub> and WSe<sub>2</sub>/GaSe heterojunctions.<sup>[39,40]</sup>

Figure 2(d) plots the photoresponsivity ( $R = I_{ph}/PS$ ) of the heterostructure at different applied voltages as a function of the incident laser power  $P$  and  $\lambda = 1064 \text{ nm}$ . Here  $S$  is the in-plane area ( $\sim 400 \text{ }\mu\text{m}^2$ ) of the heterostructure device. The photoresponsivity increases with increasing reverse bias, reaching a value of  $R = 65.56 \text{ mA W}^{-1}$  at  $V_{ds} = -0.20 \text{ V}$  and  $P = 12.50 \text{ mW cm}^{-2}$ . The photoresponsivity remains high at  $V_{ds} = 0 \text{ V}$ :  $R = 12.38 \text{ mA W}^{-1}$ , which is larger than that reported for MoTe<sub>2</sub> layers.<sup>[41]</sup> The corresponding photodetectivity  $D^*$  and photoconductive gain  $g$  are plotted for different applied biases and powers in **Figure S2**. The photodetectivity has a value of  $2.24 \times 10^{10}$  Jones at  $P = 12.50 \text{ mW cm}^{-2}$  and  $V_{ds} = 0 \text{ V}$ . This

corresponds to a photoconductive gain of  $g \sim 0.2$ . The photoresponse retains similar characteristics at different wavelengths (**Figure S3**) with a photoresponsivity of up to  $R = 27.64$  mA W<sup>-1</sup> at  $\lambda = 550$  nm and  $P = 12.50$  mW cm<sup>-2</sup>. Thus rectification and photovoltaic effects can be clearly observed in MoTe<sub>2</sub> layers with vertical asymmetric graphene contacts. The non-zero open-circuit voltage ( $V_{oc}$ ) and short-circuit current ( $I_{sc}$ ) increase with increasing laser power (**Figure S4(a-b)**). Heterostructure devices based on MoTe<sub>2</sub> layers of different thickness (from  $\sim 8$  to 21 nm) show a similar behavior (**Figure S5**) with the larger photoresponsivity being observed in the thicker layers (Table S1). For photodetectors based on MoTe<sub>2</sub> with symmetric exfoliated graphene contacts, the photoresponse is instead significantly weaker (**Figure S6**).

**Figure 3(a)** shows the normalized spectral response of the heterostructure at different illumination wavelengths (under the same power  $P = 0.63$  W cm<sup>-2</sup>). It reveals a broad photoresponse from the VIS to the NIR range ( $\lambda = 400 - 1400$  nm) with two clear peaks around  $\lambda \sim 600$  nm and 1150 nm. The peak at  $\lambda \sim 1150$  nm corresponds to the excitonic absorption associated with the lowest direct optical transition at the K-point of the Brillouin zone.<sup>[5,42]</sup> The peak at  $\lambda \sim 600$  nm arises from high energy excitonic transitions influenced by interlayer interactions.<sup>[5,43]</sup> A similar peak was also observed in the reflectance spectra of thin MoTe<sub>2</sub> layers.<sup>[5]</sup> The weak photoresponse at long wavelengths ( $\lambda \sim 1400$  nm) is assigned to the optical absorption from band tail states due to charge traps.<sup>[8,9]</sup>

To investigate the photoresponse in further detail, we carried out a series of measurements of the spatially resolved photovoltage maps. These were obtained by scanning a focused laser beam across the plane of the device without any externally applied voltage. Figure 3(b) shows the optical image of the heterostructure. A larger optical image of the device that includes the Ta/Au metal contacts is in **Figure S7**. The corresponding normalized photovoltage maps at  $\lambda =$

550 nm and 1064 nm are shown in Figure 3(c) and (d), respectively. In each Figure, the different parts of the heterostructure are marked in different colors: the bottom exfoliated graphene is marked with a white solid line; the MoTe<sub>2</sub> flake is marked with a yellow solid line, and the top CVD graphene is highlighted by a blue solid line. As shown in Figure 3(c) and (d), the photovoltage is non-uniform and is enhanced in the region of the heterostructures where all layers overlap. This enhancement was not observed in previous studies of MoTe<sub>2</sub> with symmetric CVD graphene electrodes in the literature.<sup>[41]</sup> Also, in our samples, regions with exfoliated graphene/MoTe<sub>2</sub> and MoTe<sub>2</sub>/CVD graphene, the photovoltage is much weaker. The measured photovoltage is positive in all regions, implying the existence of a built-in electric field pointing in the same direction, *e.g.* from the bottom exfoliated graphene to MoTe<sub>2</sub> in exfoliated graphene/MoTe<sub>2</sub>, from the bottom exfoliated graphene to CVD graphene in exfoliated graphene/MoTe<sub>2</sub>/CVD graphene, and from MoTe<sub>2</sub> to CVD graphene in MoTe<sub>2</sub>/CVD graphene.

To estimate the built-in electric field,  $E_{bi}$ , in the heterostructure, we fabricated and measured the transfer characteristics of FETs based on individual MoTe<sub>2</sub>, exfoliated graphene, and CVD-graphene layers on a SiO<sub>2</sub>/Si substrate. According to the transfer curves in **Figure S8**, CVD graphene is *p*-type, exfoliated graphene is *n*-type and multi-layer MoTe<sub>2</sub> is *p*-type.

The Fermi energy,  $E_F$ , for monolayer graphene, is derived from equation (1):<sup>[39,44,45]</sup>

$$E_F = \text{sign}(V_g - V_D) \hbar |v_F| \sqrt{(\pi \epsilon \epsilon_0 / t e) |V_g - V_D|} . \quad (1)$$

Here  $E_F$  is measured relative to the neutrality point of the graphene band structure,  $V_g$  is the back gate voltage on the Si-substrate,  $V_D$  is the charge neutrality point voltage from the transfer curves of graphene,  $v_F \approx 10^6 \text{ m s}^{-1}$  is the Fermi velocity,  $\epsilon_0$  is the permittivity of free space,  $\epsilon = 3.9$  is the dielectric constant of SiO<sub>2</sub>,  $e$  is the electron charge and  $t = 300 \text{ nm}$  is the thickness



of SiO<sub>2</sub>.<sup>[39,44,45]</sup>

We set the Dirac point of graphene at -4.55 eV relative to the vacuum level. From the measured transfer curves in Figure S6, we derive that the Fermi level of CVD graphene is at an energy of 0.19 eV below the Dirac point, *i.e.*  $E_{Fp} = -4.74$  eV, at  $V_g = 0$  V. We obtain a similar estimate of doping level from the analysis of the Raman spectra (Supplementary Material S9). For *n*-type exfoliated multilayer graphene, we obtain an upper estimate of the Fermi level by using equation (1),  $E_{Fn} = -4.44$  eV. Thus from  $E_{Fp} = -4.74$  eV and  $E_{Fn} < -4.44$  eV, we infer a built-in electric field  $E_{bi} = (E_{Fn} - E_{Fp})/el < 150$  kV cm<sup>-1</sup>, where  $l = 15$  nm is the thickness of the MoTe<sub>2</sub> layer. On the other hand, since exfoliated graphene is *n*-type, its Fermi level should be above the Dirac point, *i.e.*  $E_{Fn} > -4.55$  eV. Thus we conclude that the built-in electric field should be within the range  $127 \text{ kV cm}^{-1} < E_{bi} < 150 \text{ kV cm}^{-1}$ . The corresponding energy band diagram of the heterostructure at equilibrium is shown in **Figure 4(a)**. The junction can work under different conditions including the photovoltaic mode without any applied voltage (Figure 4(b)) and the photoconductive mode under reverse bias (Figure 4(c)). At zero bias, the built-in electric field points in same direction at the CVD graphene/MoTe<sub>2</sub> and exfoliated graphene/MoTe<sub>2</sub> interfaces. Thus the photoresponse of the regions where all layers overlap is stronger than in other regions. This is consistent with our scanning photovoltage maps (Figure 3(c-d)) and studies of additional devices including MoTe<sub>2</sub> with symmetric exfoliated graphene contacts and MoTe<sub>2</sub> with symmetric CVD graphene contacts (Figure 1(d)). The curves show nonlinear characteristics, which confirms that contact barriers exist at the interfaces of CVD graphene/MoTe<sub>2</sub> and exfoliated graphene/MoTe<sub>2</sub>. Finally, we note that under a reverse bias voltage, the externally applied electric-field points in the same direction as the built-in electric field. At  $V_{ds} = -0.2$  V, the electric field almost doubles, leading to a larger photocurrent, as

measured experimentally (Figure 2).

The stability and speed of the photoresponse are crucial figures of merit of a photodetector. **Figure 5(a)** and **(b)** show the temporal response of the photocurrent. This is obtained with a square-wave modulation of the light intensity for different powers ( $P = 0.31, 1.25, \text{ and } 3.13 \text{ W cm}^{-2}$ ) at  $\lambda = 1064 \text{ nm}$ . Under zero or reverse biases, the photocurrent can be switched on and off repeatedly and reproducibly. This switching behavior was also observed for photoexcitation under different laser wavelengths ( $\lambda = 400, 550, 635, 800, \text{ and } 1064 \text{ nm}$ ) at zero bias (**Figure S9**). Also, the heterostructure exhibits a fast dynamic response (**Figure 5(c)** and **(d)**). To study the temporal response of the current, the heterostructure was illuminated with pulsed light generated by a light-emitting diode driven by a square-wave signal generator. The dynamic response for the rise and decay of the photocurrent is well described by the equations  $I(t)=I_0[1 - \exp(-t/\tau_r)]$  and  $I(t)=I_0 \exp(-t/\tau_d)$ , where  $\tau_r$  and  $\tau_d$  are the time constants for the rise and decay of the current. By fitting the rising and falling edges of the current versus time in **Figure 5(c)**, we derive  $\tau_r = 16.58 \mu\text{s}$  and  $\tau_d = 14.96 \mu\text{s}$  at  $V_{ds} = 0 \text{ V}$ . A faster photoresponse with  $\tau_r = 6.15 \mu\text{s}$  and  $\tau_d = 4.35 \mu\text{s}$  is obtained at  $V_{ds} = -0.20 \text{ V}$ . This faster dynamics is assigned to the enhanced electric field of the heterostructure by the applied reverse bias.<sup>[33]</sup> As summarized in **Table 1**, the measured photoresponse times are shorter than those reported for MoTe<sub>2</sub> based FETs and several other heterostructure photodetectors in the literature.<sup>[1,9,17,46-52]</sup> We assign the improved photoresponse to the short transport channel and enhanced built-in electric field of the heterostructure.

### 3. Conclusions

In summary, we have demonstrated high-performance heterostructure photodetectors

based on multilayer MoTe<sub>2</sub> with vertical asymmetric graphene contacts. The heterostructure not only exhibits a broadband photoresponse from  $\lambda = 400$  to 1400 nm, but also shows high responsivity of up to  $R = 27.64 \text{ mA W}^{-1}$  under zero bias. Thus even without any externally applied voltage, the photo-generated carriers are efficiently separated by the built-in electric field of the heterostructure. The photoresponse is significantly enhanced in the vertical overlapping region (exfoliated graphene/MoTe<sub>2</sub>/CVD graphene). Furthermore, the heterostructure shows a fast temporal response with decay and rise times in the microsecond range. The improved photoresponse indicate that van der Waals heterostructures with asymmetric graphene contacts are promising candidates for high-speed and self-powered optoelectronic devices. Research on the epitaxial growth of graphene and the controlled doping of graphene are still in their infancy. Progress in these important areas has the potential to further enhance the performance of these device and accelerate the use of asymmetric graphene contacts for a wide range of optoelectronic devices.

#### **4. Experimental sections**

**Device fabrication.** The multilayer graphene was mechanically exfoliated using adhesive tape from a bulk single crystal. We find and identify the approximate thickness of the graphene flakes by optical contrast using an optical microscope. The accurate thickness of the flakes is determined by using atomic force microscopy (AFM). The optical microscope has a 20 $\times$  objective lens and a 10 $\times$  eyepiece, which enable us to identify clearly areas down to 2  $\mu\text{m} \times 2 \mu\text{m}$ . We use a three-axis water hydraulic micromanipulator (Narishige, Japan) to transfer a multilayer graphene flake (bottom contact) on a Si/SiO<sub>2</sub> substrate (300 nm-thick SiO<sub>2</sub>). The moving accuracy of the three-axis water hydraulic micromanipulator is 1  $\mu\text{m}$ . Using the same

mechanical exfoliation and transfer method, a MoTe<sub>2</sub> flake is then transferred onto the bottom graphene layer. Finally, a CVD graphene microstamp is transferred onto the MoTe<sub>2</sub> sheet to form the top contact. The CVD graphene was synthesized on a Cu substrate. By wet-etching, electron beam lithography and oxygen plasma etching, CVD-graphene is processed into microstamps prior to the mechanical transfer. Metallic contacts (Ta/Au) are fabricated on the substrate using standard photoetching, magnetron sputtering and lift off. All mechanical exfoliation and transfer processes are conducted inside a glove box. Our methods for transferring and stacking the layers are described in the literature.<sup>[32,53,54]</sup>

**Electrical and opto-electrical studies.** The  $I_{ds} - V_{ds}$  curves were measured by an Agilent Technology B1500A Semiconductor Device Analyzer. The measurement resolution of the Semiconductor Device Analyzer was down to 0.1 fA and 0.5  $\mu$ V. The monochromatic illumination was provided by a Zolix Omni- $\lambda$ 300 monochromator coupled to a Fianium WhiteLase Supercontinuum Laser Source. The Fianium WhiteLase Supercontinuum Laser Source generates laser wavelengths from 400 nm to 2400 nm whose power can be controlled accurately. We used an optical power meter (PM100D ,Thorlabs) to monitor the output laser power on the sample. A objective lens (100 $\times$ , Olympus), a light chopper, a micromechanical stage (MAX381, Thorlabs) and a lock-in amplifier (SR830, Stanford Research Systems) were used to carry out spatially resolved photovoltage mapping. A digital oscilloscope and pulsed light were used to investigate the response time. The pulsed light was generated by a light-emitting diode driven by a square-wave signal generator

## **Supporting Information**

Supporting Information is available from the Wiley Online Library or from the author.

## **Acknowledgments**

This work was supported by National Key R&D Program of China No. 2017YFA0303400, by the NSFC Grant No. 61774144, by the EU Graphene Flagship Project, and the Engineering and Physical Sciences Research Council (Grant No. EP/M012700/1). The Project was sponsored by CAS, Grant NO. QYZDY-SSW-JSC020, XDPB12, and XDB28000000, and also by K C Wong Education Foundation.

## **Conflict of Interest**

The authors declare no conflict of interest.

## References

- [1] W. Yu, S. Li, Y. Zhang, W. Ma, T. Sun, J. Yuan, K. Fu, Q. Bao. *Small* **2017**, 13, 1700268.
- [2] M. Buscema, J. O. Island, D. J. Groenendijk, S. I. Blanter, G. A. Steele, H. S. van der Zant, A. Castellanos-Gomez. *Chem. Soc. Rev.* **2015**, 44, 3691.
- [3] A. Pospischil, T. Mueller. *Appl. Sci.* **2016**, 6, 78.
- [4] K. F. Mak, J. Shan. *Nature Photon.* **2016**, 10, 216.
- [5] C. Ruppert, O. B. Aslan, T. F. Heinz. *Nano Lett.* **2014**, 14, 6231.
- [6] I. G. Lezama, A. Arora, A. Ubaldini, C. Barreteau, E. Giannini, M. Potemski, A. F. Morpurgo. *Nano Lett.* **2015**, 15, 2336.
- [7] I. G. Lezama, A. Ubaldini, M. Longobardi, E. Giannini, C. Renner, A. B. Kuzmenko, A. F. Morpurgo. *2D Mater.* **2014**, 1, 021002.
- [8] H. Huang, X. Wang, P. Wang, G. Wu, Y. Chen, C. Meng, L. Liao, J. Wang, W. Hu, H. Shen. *RSC Adv.* **2016**, 6, 87416.
- [9] H. Huang, J. Wang, W. Hu, L. Liao, P. Wang, X. Wang, F. Gong, Y. Chen, G. Wu, W. Luo. *Nanotechnology* **2016**, 27, 445201.
- [10] F. Yan, Z. Wei, X. Wei, Q. Lv, W. Zhu, K. Wang. *Small Methods* **2018**, 2, 1700349.
- [11] A. Beal, H. Hughes. *J. Phys. C: Solid State Physics* **1979**, 12, 881.
- [12] F. H. Koppens, T. Mueller, P. Avouris, A. C. Ferrari, M. S. Vitiello, M. Polini. *Nature Nanotech.* **2014**, 9, 780.
- [13] K. Zhang, T. Zhang, G. Cheng, T. Li, S. Wang, W. Wei, X. Zhou, W. Yu, Y. Sun, P. Wang. *ACS nano* **2016**, 10, 3852.
- [14] M. Dai, H. Chen, R. Feng, W. Feng, Y. Hu, H. Yang, G. Liu, X. Chen, J. Zhang, C.-Y. Xu. *ACS nano* **2018**, 12, 8739.
- [15] D. Qi, Q. Wang, C. Han, J. Jiang, Y. Zheng, W. Chen, W. Zhang, A. T. S. Wee. *2D Mater.* **2017**, 4, 045016.
- [16] C. Zhou, S. Raju, B. Li, M. Chan, Y. Chai, C. Y. Yang. *Adv. Funct. Mater.* **2018**, 28, 1802954.
- [17] M. Luo, F. Wu, M. Long, X. Chen. *Nanotechnology* **2018**, 29, 444001.
- [18] Y. Xu, C. Cheng, S. Du, J. Yang, B. Yu, J. Luo, W. Yin, E. Li, S. Dong, P. D. Ye. *ACS nano* **2016**.

- [19] T. Mueller, F. Xia, P. Avouris. *Nature Photon.* **2010**, 4, 297.
- [20] L. Zheng, L. Zhongzhu, S. Guozhen. *J. Semicond.* **2016**, 37, 091001.
- [21] J.-J. Chen, Q. Wang, J. Meng, X. Ke, G. V. Tendeloo, Y.-Q. Bie, J. Liu, K. Liu, Z.-M. Liao, D. Sun. *ACS nano* **2015**, 9, 8851.
- [22] G. W. Mudd, S. A. Svatek, L. Hague, O. Makarovskiy, Z. R. Kudrynskiy, C. J. Mellor, P. H. Beton, L. Eaves, K. S. Novoselov, Z. D. Kovalyuk. *Adv. Mater.* **2015**, 27, 3760.
- [23] G. Jo, M. Choe, S. Lee, W. Park, Y. H. Kahng, T. Lee. *Nanotechnology* **2012**, 23, 112001.
- [24] S. Pang, Y. Hernandez, X. Feng, K. Müllen. *Adv. Mater.* **2011**, 23, 2779.
- [25] Y. Zhu, S. Murali, W. Cai, X. Li, J. W. Suk, J. R. Potts, R. S. Ruoff. *Adv. Mater.* **2010**, 22, 3906.
- [26] J. Liu, N. Guo, X. Xiao, K. Zhang, Y. Jia, S. Zhou, Y. Wu, Q. Li, L. Xiao. *Nanoscale Res. Lett.* **2017**, 12, 603.
- [27] J. Miao, S. Zhang, L. Cai, C. Wang. *Adv. Electron. Mater.* **2016**, 2, 1500346.
- [28] S. Kallatt, S. Nair, K. Majumdar. *Small* **2018**, 14, 1702066.
- [29] C.-H. Liu, Y.-C. Chang, T. B. Norris, Z. Zhong. *Nature Nanotech.* **2014**, 9, 273.
- [30] B. Wang, S. Yang, C. Wang, M. Wu, L. Huang, Q. Liu, C. Jiang. *Nanoscale* **2017**, 9, 10733.
- [31] A. Pezeshki, S. H. H. Shokouh, T. Nazari, K. Oh, S. Im. *Adv. Mater.* **2016**, 28, 3216.
- [32] A. Castellanos-Gomez, M. Buscema, R. Molenaar, V. Singh, L. Janssen, H. S. Van Der Zant, G. A. Steele. *2D Mater.* **2014**, 1, 011002.
- [33] F. Yan, L. Zhao, A. Patané, P. Hu, X. Wei, W. Luo, D. Zhang, Q. Lv, Q. Feng, C. Shen. *Nanotechnology* **2017**, 28, 27LT01.
- [34] A. C. Ferrari, J. Meyer, V. Scardaci, C. Casiraghi, M. Lazzeri, F. Mauri, S. Piscanec, D. Jiang, K. Novoselov, S. Roth. *Phys. Rev. Lett.* **2006**, 97, 187401.
- [35] L. Cançado, A. Reina, J. Kong, M. Dresselhaus. *Phys. Rev. B* **2008**, 77, 245408.
- [36] L. Malard, M. Pimenta, G. Dresselhaus, M. Dresselhaus. *Phys. Rep.* **2009**, 473, 51.
- [37] J. O. Island, S. I. Blanter, M. Buscema, H. S. van der Zant, A. Castellanos-Gomez. *Nano Lett.* **2015**, 15, 7853.
- [38] A. Abderrahmane, P.-G. Jung, N.-H. Kim, P. J. Ko, A. Sandhu. *Opt. Mater. Express* **2017**, 7, 587.

- [39] X. Wei, F. Yan, Q. Lv, C. Shen, K. Wang. *Nanoscale* **2017**, 9, 8388.
- [40] Y. Xue, Y. Zhang, Y. Liu, H. Liu, J. Song, J. Sophia, J. Liu, Z. Xu, Q. Xu, Z. Wang. *Acs Nano* **2015**, 10, 573.
- [41] K. Zhang, X. Fang, Y. Wang, Y. Wan, Q. Song, W. Zhai, Y. Li, G. Ran, Y. Ye, L. Dai. *ACS Appl. Mater. Interfaces* **2017**, 9, 5392.
- [42] J. Yang, T. Lu, Y. W. Myint, J. Pei, D. Macdonald, J.-C. Zheng, Y. Lu. *ACS nano* **2015**, 9, 6603.
- [43] J. A. Wilson, A. Yoffe. *Adv. Phys.* **1969**, 18, 193.
- [44] K. Roy, M. Padmanabhan, S. Goswami, T. P. Sai, G. Ramalingam, S. Raghavan, A. Ghosh. *Nature Nanotech.* **2013**, 8, 826.
- [45] A. Gao, E. Liu, M. Long, W. Zhou, Y. Wang, T. Xia, W. Hu, B. Wang, F. Miao. *Appl. Phys. Lett.* **2016**, 108, 223501.
- [46] W. Feng, Z. Jin, J. Yuan, J. Zhang, S. Jia, L. Dong, J. Yoon, L. Zhou, R. Vajtai, J. M. Tour. *2D Mater.* **2018**, 5, 025008.
- [47] Y. Wang, X. Huang, D. Wu, R. Zhuo, E. Wu, C. Jia, Z. Shi, T. Xu, Y. Tian, X. Li. *J. Mater. Chem. C* **2018**, 6, 4861.
- [48] Q. Lv, F. Yan, X. Wei, K. Wang. *Adv. Opt. Mater.* **2018**, 6, 1700490.
- [49] M. Kuiri, B. Chakraborty, A. Paul, S. Das, A. Sood, A. Das. *Appl. Phys. Lett.* **2016**, 108, 063506.
- [50] A. Li, Q. Chen, P. Wang, Y. Gan, T. Qi, P. Wang, F. Tang, J. Z. Wu, R. Chen, L. Zhang. *Adv. Mater.* **2018**, 1805656.
- [51] Y. Chen, X. Wang, G. Wu, Z. Wang, H. Fang, T. Lin, S. Sun, H. Shen, W. Hu, J. Wang. *Small* **2018**, 14, 1703293.
- [52] M. A. Bhuiyan, Z. R. Kudrynskyi, D. Mazumder, J. D. Greener, O. Makarovskiy, C. J. Mellor, E. E. Vdovin, B. A. Piot, I. I. Lobanova, Z. D. Kovalyuk. *Adv. Funct. Mater.* **2019**, 1805491.
- [53] J.-J. Chen, J. Meng, Y.-B. Zhou, H.-C. Wu, Y.-Q. Bie, Z.-M. Liao, D.-P. Yu. *Nature Commun.* **2013**, 4, 1921.
- [54] Y. Q. Bie, Y. B. Zhou, Z. M. Liao, K. Yan, S. Liu, Q. Zhao, S. Kumar, H. C. Wu, G. S. Duesberg, G. L. Cross. *Adv. Mater.* **2011**, 23, 3938.



## Figures

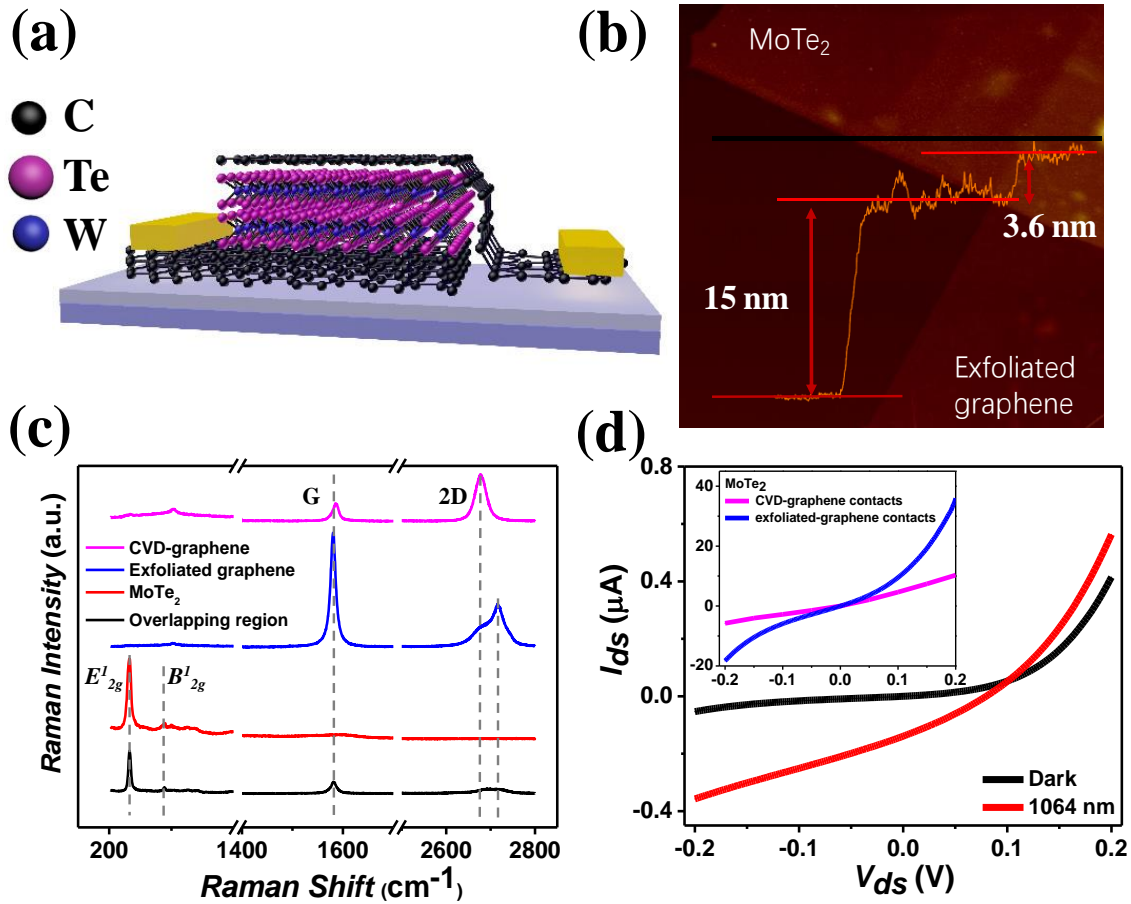


**Figure 1** (a) Schematic diagram of multilayer MoTe<sub>2</sub> with asymmetric graphene contacts. (b) AFM image of one typical device. The inset is the AFM z-profile showing the thickness of the MoTe<sub>2</sub> and bottom exfoliated graphene layers. (c) Raman spectra for different regions of the heterostructure including CVD-graphene, exfoliated graphene, MoTe<sub>2</sub>, and the vertical overlapping region. The diameter of the laser spot for the Raman studies is approximately 1.5  $\mu\text{m}$ . (d) Current-voltage  $I_{ds} - V_{ds}$  curves in the dark and under illumination with a laser of wavelength  $\lambda = 1064$  nm and power  $P = 3.13$  W  $\text{cm}^{-2}$ . The diameter of the laser beam is about 45  $\mu\text{m}$ , which is larger than the device size. The inset shows the  $I_{ds} - V_{ds}$  curves in the dark of MoTe<sub>2</sub> photodetectors with symmetric graphene contacts.

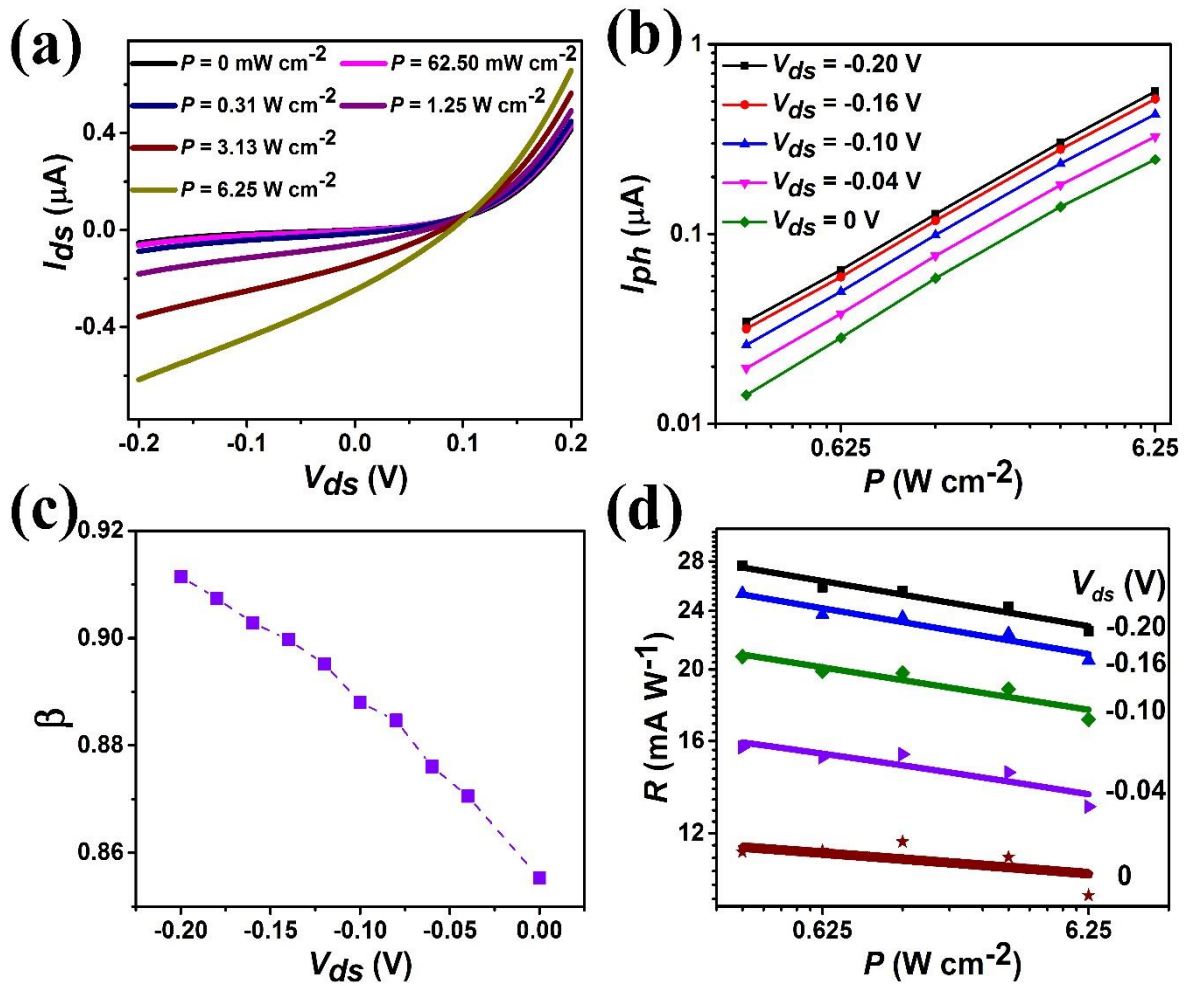


**Figure 2** (a)  $I_{ds} - V_{ds}$  curves with illumination at various laser powers  $P$  at room temperature ( $\lambda = 1064$  nm). (b) Photocurrent  $I_{ph}$  as a function of  $P$  at different reverse biases  $V_{ds}$ . (c) Dependence of the exponent  $\beta$  on the reverse bias ( $\lambda = 1064$  nm). (d) Photoresponsivity  $R$  as a function of  $P$  at different  $V_{ds}$ . The diameter of the laser spot is about  $45 \mu\text{m}$ , which is larger than the device size.

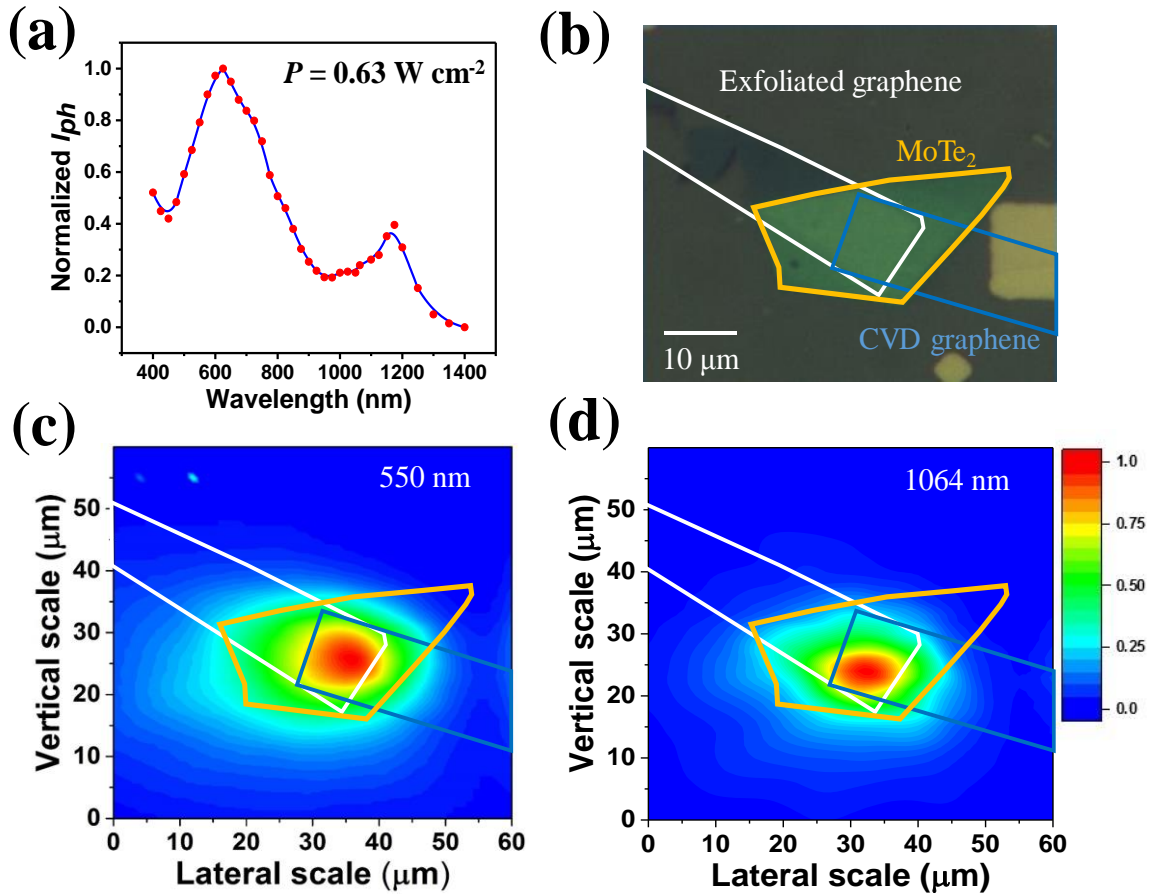


**Figure 3** (a) Normalized  $I_{ph}$  as a function of illumination wavelength from 400 to 1400 nm at zero bias, with incident power  $P = 0.623 \text{ W cm}^{-2}$ . (b) Optical microscope image of the heterostructure. (c) and (d) Normalized photovoltage maps at zero bias of multilayer  $\text{MoTe}_2$  with asymmetric graphene contacts. The maps are obtained by scanning a focused laser beam with wavelength  $\lambda = 550 \text{ nm}$  and  $1064 \text{ nm}$ , respectively ( $P = 20 \mu\text{W}$ ). The white, yellow and blue lines demarc different layers: exfoliated graphene,  $\text{MoTe}_2$  and CVD graphene, respectively. The largest photoresponse is observed in the vertical overlapping region (exfoliated graphene/ $\text{MoTe}_2$ /CVD graphene). The laser beam is focused by a  $100\times$  microscope objective to a spot of diameter  $d \sim 1.5 \mu\text{m}$ .

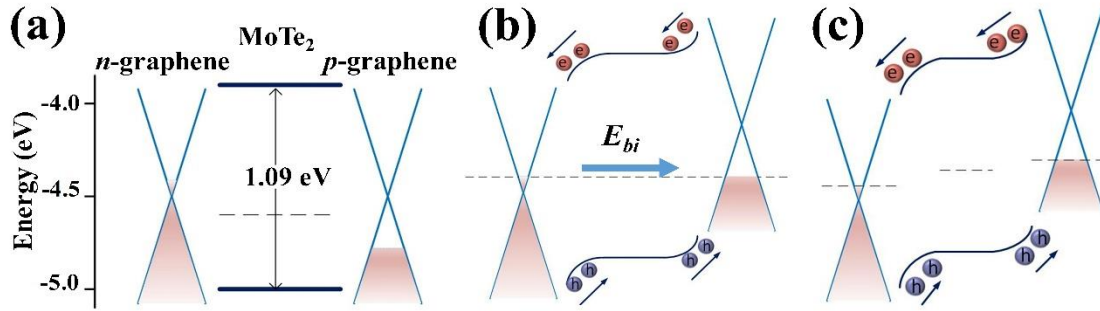


**Figure 4** (a) Energy band alignment for isolated  $n$ -type exfoliated graphene,  $p$ -type MoTe<sub>2</sub>, and  $p$ -type CVD graphene. (b) and (c) Energy band diagrams of the heterostructure under illumination at zero bias and reverse bias, respectively. The dotted line represents the Fermi level. The blue arrow shows the direction of the built-in electric field.

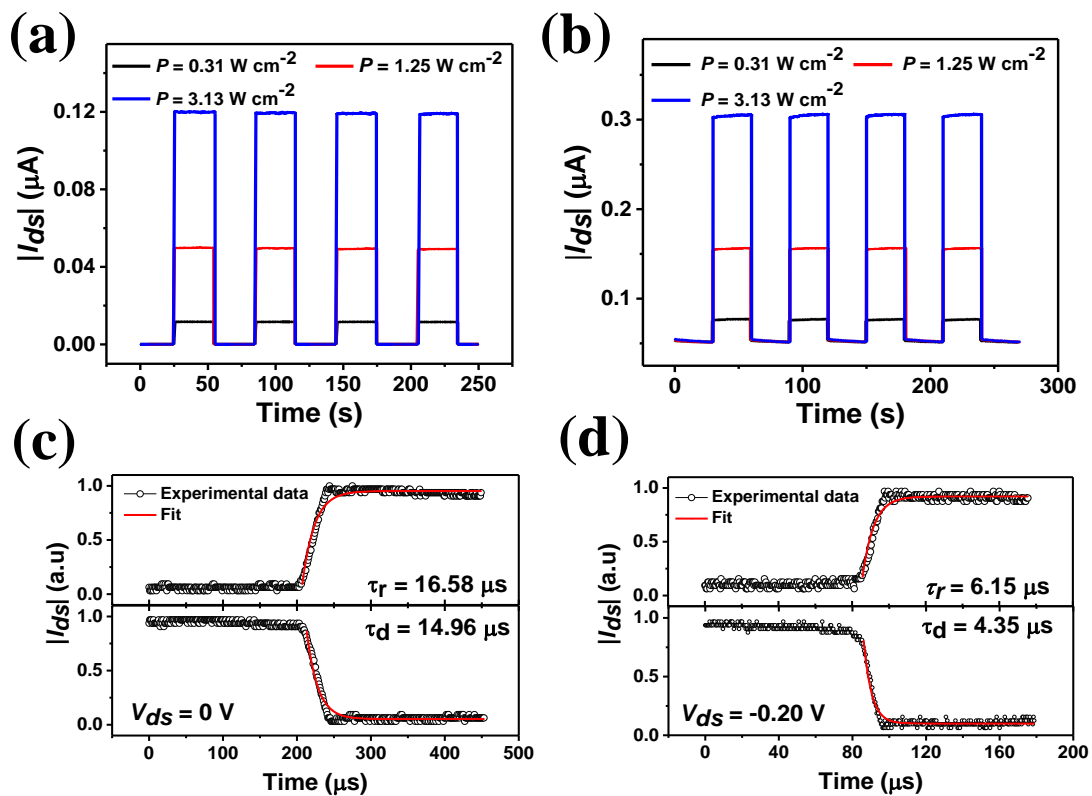


**Figure 5** (a) and (b) Reproducible photo-switching of the heterostructure with 1064 nm illumination under different powers ( $P = 0.31, 1.25, \text{ and } 3.13 \text{ W cm}^{-2}$ ) at  $V_{ds} = 0 \text{ V}$  and  $-0.20 \text{ V}$ , respectively. (c) and (d) Temporal dependence of the photocurrent at  $V_{ds} = 0 \text{ V}$  and  $V_{ds} = -0.20 \text{ V}$  at room temperature. The red solid lines are fits to the data.

**Table 1** Comparison of our MoTe<sub>2</sub>-based photodetector with other photodetectors in the literature.

Structure	voltage [V]	wavelength [nm]	Responsivity [A W <sup>-1</sup> ]	Response time [ms]	Reference
MoTe <sub>2</sub>	10	1060	0.024	1.6	[9]
MoTe <sub>2</sub> /graphene	1	1064	970.82	78	[1]
MoTe <sub>2</sub> /graphene	-2	532	0.02	30	[49]
MoTe <sub>2</sub> /graphene/SnS <sub>2</sub>	1	1064	2.6×10 <sup>3</sup>	24	[50]
MoTe <sub>2</sub> /MoS <sub>2</sub>	0	637	0.44	0.06	[51]
Graphene/InSe/graphene	0.1	633	10 <sup>6</sup>	1	[52]
Graphene/Ta <sub>2</sub> O <sub>5</sub> /Graphene	1	532	1000	> 1	[29]
Au/InSe/In	0	365	0.11	75	[14]
Graphene/MoTe <sub>2</sub> /Au	0.1	532	0.046	96	[15]
MoTe <sub>2</sub> with asymmetric Au contact form	0	637	NA	0.13	[26]
MoTe <sub>2</sub> with asymmetric graphene contacts	-0.2	1064	0.066	6.15×10 <sup>-3</sup>	This work